



Electrostatic confinement of electrons in graphene nanoribbons

Xinglan Liu,¹ Jeroen B. Oostinga,^{1,2} Alberto F. Morpurgo,² and Lieven M. K. Vandersypen¹

¹Kavli Institute of NanoScience, Delft University of Technology, P.O. Box 5046, 2600 GA Delft, The Netherlands

²DPMC and GAP, University of Geneva, 24 quai Ernest Ansermet, Geneva CH1211, Switzerland

(Received 3 September 2009; published 28 September 2009)

Coulomb blockade is observed in a graphene nanoribbon device with a top gate. When two pn junctions are formed via the back gate and the local top gate, electrons are confined between the pn junctions which act as the barriers. When no pn junctions are induced by the gate voltages, electrons are still confined, as a result of strong disorder, but in a larger area. Measurements on five other devices with different dimensions yield consistent results.

DOI: [10.1103/PhysRevB.80.121407](https://doi.org/10.1103/PhysRevB.80.121407)

PACS number(s): 85.35.-p, 72.80.Rj, 73.20.Fz, 81.05.Uw

Confinement of the Dirac particles is of particular importance for the realization of nanoelectronic devices in graphene such as quantum dots.¹ These would enable one to perform single-level spectroscopy of Dirac particles, study their spin and valley degrees of freedom, and explore their potential for quantum coherent control.² In conventional semiconductors, particles can be confined by potential barriers created via electrostatic gates. This approach permits independent control of the number of electrons on the island, the tunnel coupling between the island and the reservoirs, as well as the tunnel coupling between neighboring islands. Such flexibility and versatility has been instrumental for a wide variety of mesoscopic experiments. In graphene, this approach normally fails, due to the absence of a bandgap and the presence of Klein tunneling.^{3,4} In previous studies, graphene has been etched into small islands, separated from the reservoir by narrow constrictions,⁵⁻⁷ but here it is difficult to tune the barriers. Alternatively, a bandgap could be created in graphene first, so that electrostatic gates can again be used for confinement. Theoretically, a bandgap is predicted in graphene nanoribbons (GNRs) due mainly to quantum confinement.⁸⁻¹⁰ Experimentally, a transport gap has indeed been observed in GNR devices,¹¹⁻¹⁴ but its origin is still under debate.

Here we experimentally investigate GNR devices with a local top gate (TG) and a global back gate (BG) where the transport gap in the GNR enables electrostatic confinement by the gates. Electrons are confined in an island where the barriers are formed by the pn -junctions induced at the two edges of the TG, as demonstrated by the capacitance analysis of the measured Coulomb blockade. On the other hand, when no pn -junctions were induced by the gates, Coulomb blockade was also observed, showing a larger confinement area. Here the island may be due to Anderson localization. Consistent results were found in five other devices with different dimensions.

Six devices (A to F) are fabricated on graphene flakes deposited on a substrate by mechanical exfoliation of natural graphite.¹⁵ The substrate consists of highly p -doped silicon, acting as a BG, capped by 285 nm of SiO_2 . From their optical contrast against the substrate, we estimate that the flakes are single layer.¹⁶ Three electron-beam lithography steps were used for patterning the devices. First, selected graphene flakes are patterned into GNRs, using PMMA as an etching

mask and an Ar plasma for etching (for device F an O_2 plasma was used). Next we pattern a single top gate across each ribbon. The TG consists of 10/5/40 nm thick evaporated $\text{SiO}_2/\text{Ti}/\text{Au}$, and it covers only part of the ribbon, denoted as segment I [see Fig. 1(a)]. The remainder of the ribbon (segments II) connects to wider pieces of graphene, which are contacted by 10/40-nm-thick Ti/Au source (S) and drain (D) electrodes. The device is schematically illustrated in Fig. 1(b), and the relevant device dimensions are given in Table I.

All measurements were performed in a ^3He system at a base temperature of 350 mK, unless stated otherwise. We measured the two terminal resistance through the top gated GNR devices by applying a dc voltage bias, V_{bias} , on the source electrode and measuring the current at the drain electrode.

By tuning the BG and TG voltages, we can shape the potential landscape along the ribbon. Figure 1(c) shows the low bias conductance of device A as a function of V_{BG} and V_{TG} at $T=4$ K. Along the dark vertical band, the conductance is suppressed as E_F is within the transport gap in seg-

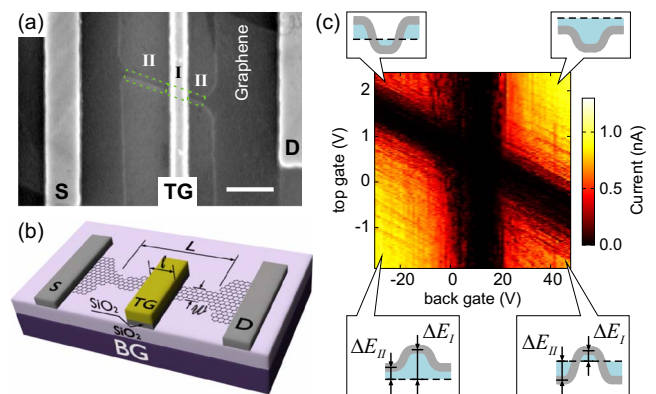


FIG. 1. (Color online) (a) Scanning electron microscope image of device E (scale bar 300 nm). The green dashed lines indicate segments I and II discussed in the text. (b) Schematic drawing of the device. (c) Current as a function of the back gate and top gate voltages for device A at $V_{bias}=150 \mu\text{V}$ and $T=4$ K. The insets illustrate the potential landscapes that are created in the four corners of the plot. They represent energy diagrams along the ribbon length, where the gray band indicates the transport gap and the dashed lines represent the Fermi level E_F . $\Delta E_{I(II)}$ indicates the doping level in segment I (II).

TABLE I. The dimensions of devices A to F. The TG dielectric is $d=10$ -nm-thick SiO_2 for all devices.

	Label (nm)	A	B	C	D	E	F
GNR width	w	60	50	50	50	40	40
GNR length	L	2000	1500	1000	700	520	520
TG width	l	500	400	200	140	100	50

ment II. Along the dark diagonal band, the TG and BG dope the graphene with opposite polarity and E_F lies in the transport gap in segment I. At zero gate voltages, the device was unintentionally hole doped.

In the lower right (upper left) corner of Fig. 1(c), the ribbon is in a npn (pnp) configuration. In this regime, holes (electrons) can be confined in the area (segment I) between the two pn -junctions owing to the presence of the transport gap.^{17,18} We thus expect Coulomb blockade in the npn and pnp regimes. In the lower left (upper right) corner, the ribbon is in a $pp'p$ ($nn'n$) configuration. Here Fabry-Perot-type resonances could occur between the two steps in the potential landscape, but no Coulomb blockade is expected in an ideal ribbon, as there are no barriers. The difference in energy from E_F to the middle of the transport gap in segments I and II are denoted as ΔE_I and ΔE_{II} , respectively, which is a measure of the doping level.

In the npn configuration, we observe pronounced current peaks separated by zero-current regions as V_{TG} is swept. A representative measurement is shown in Fig. 2(d) for device B, measured in the gate voltage configuration indicated by the black arrows in Figs. 2(a) and 3(b). High bias measurements in the same range [Fig. 2(e)] show diamond-shaped regions in the $V_{bias}-V_{TG}$ plane, in which current is blocked. Both are characteristic of Coulomb blockade due to the formation of an island that is only weakly coupled to the leads.

In this device, over 700 Coulomb peaks were resolved in the range $-2 < V_{TG} < -0.2$ V, corresponding to a large change in doping level in segment I, $-360 \leq \Delta E_I \leq -240$ meV [Fig. 3(a)]. Here ΔE_I reflects the doping level in segment I [Fig. 1(c) inset], and is roughly estimated by considering the density of states of bulk graphene, $\Delta E_I = (\pm) \hbar v_F \sqrt{\pi n_I}$, where n_I is the carrier density in region I, v_F is the Fermi velocity of bulk graphene, and the (+) and (-) signs represent electron and hole doping, respectively. The spacings between neighboring peaks, ΔV_{TG}^{npn} , are shown in Fig. 3(a) (black spheres), as a function of the peak positions. The average value $\langle \Delta V_{TG}^{npn} \rangle = 2.0 \pm 0.4$ mV corresponds to a TG capacitance $C_{TG} = 70-100$ aF, close to what one would expect from simple parallel-plate capacitance between the TG and segment I, $C_{TG}^{\parallel} = \epsilon_0 \epsilon_r w l / d = 70$ aF, where $\epsilon_r = 3.9$ is the relative permittivity of SiO_2 . In addition, the capacitance to the back gate, measured to be ~ 3.9 aF, compares well to the value expected from the geometry of an island of area (wl). The agreement demonstrates that for this device, an island is formed between the two pn junctions in the npn configuration.

In addition, we measured over 100 Coulomb diamonds similar to Fig. 2(e), and the extracted addition energy E_a^{npn} for each diamond is shown in Fig. 3(a) with green (gray)

triangles. The average addition energy is $\langle E_a^{npn} \rangle = 1.0 \pm 0.4$ meV. From Fig. 3(a), no shell filling or evident top gate voltage dependence is observed in either ΔV_{TG} or E_a , but both quantities show a large spread similar to Refs. 5 and 6, due to contributions from both the level spacing and strong disorder from the ribbon edges, which is discussed further below. In all these measurements, segments II of the GNR were heavily n doped such that disorder in the leads was largely screened ($V_{BG} = +81$ V).¹⁹

Unexpectedly, Coulomb blockade was also observed when no pn -junctions are present. Figures 2(b) and 2(c) show a representative current trace and Coulomb diamonds measured from the same device in a $pp'p$ configuration indicated by the red (gray) arrows in Figs. 2(a) and 3(d). Over 1400 current peaks were observed in the range $-1 < V_{TG} < 2.2$ V, corresponding to a change in doping level ΔE_I from -430 meV to -230 meV [Fig. 3(c)]. We measured 70 Coulomb diamonds in the same range. The extracted peak spacings $\Delta V_{TG}^{pp'p}$ and addition energy $E_a^{pp'p}$ are shown in Fig.

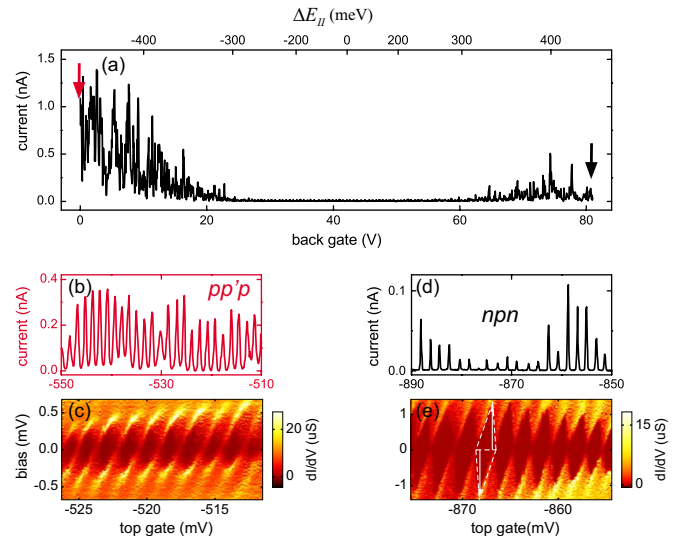


FIG. 2. (Color online) (a) Current as a function of V_{BG} for device B at $V_{TG} = -1.2$ V and $V_{bias} = 200$ μV . The top axis indicates the corresponding doping level in segment II, ΔE_{II} , estimated in the same way as ΔE_I (see text). (b) Coulomb oscillations as a function of V_{TG} in the $pp'p$ configuration. $V_{BG} = 0$ as indicated by the red (gray) arrow in (a) and $V_{bias} = 100$ μV . (c) Differential conductance dI/dV as a function of V_{TG} and V_{bias} (Coulomb diamonds), measured in the same $pp'p$ regime as (b). (d) Coulomb oscillations as a function of V_{TG} in the npn configuration. $V_{BG} = +81$ V as indicated by the black arrow in (a), and $V_{bias} = 100$ μV . (e) Coulomb diamonds measured in the same npn regime as (d). The addition energy E_a is taken as the average of the two white arrows.

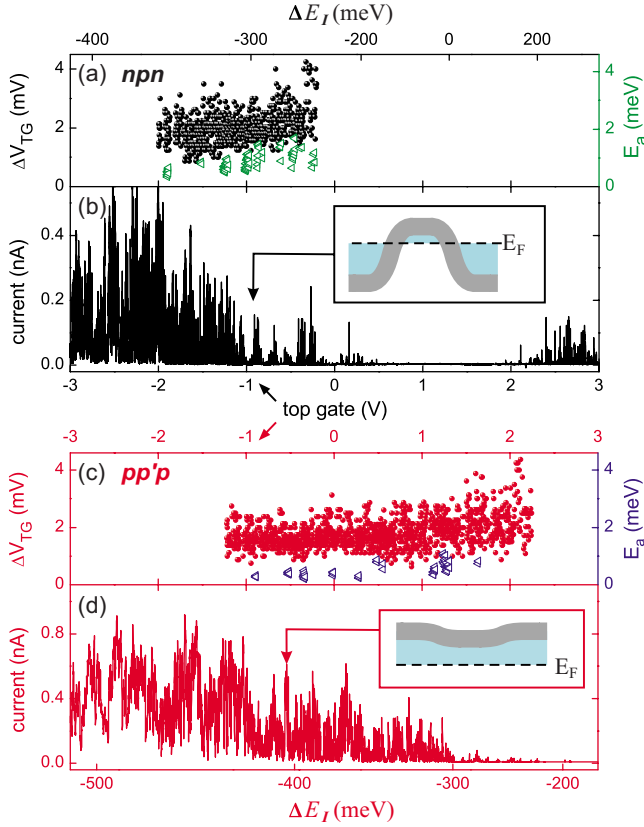


FIG. 3. (Color online) (a) ΔV_{TG} (black spheres) and E_a (green triangles) as a function of peak positions in the npn regime for device B . $V_{BG}=+81$ V. (b) Current (black line) as a function of V_{TG} at $V_{bias}=100$ μ V and $V_{BG}=+81$ V. (c) ΔV_{TG} (red spheres) and E_a (blue triangles) in the $pp'p$ regime for at $V_{BG}=0$. (d) Current (red line) as a function of V_{TG} at $V_{bias}=100$ μ V and $V_{BG}=0$. The corresponding doping level in segment I, ΔE_I , are indicated in the top axis (a) and bottom axis (d). The two insets illustrate the potential landscapes created at the gate voltage configurations where Figs. 2(b) and 2(d) are taken.

3(c) with red spheres and blue triangles, respectively. The measurements were taken at $V_{BG}=0$ [red (gray) arrow in Fig. 2(a)], such that segment II of the GNR was heavily p doped.

The average peak spacing in the $pp'p$ configuration $\langle \Delta V_{TG}^{pp'p} \rangle = 1.8 \pm 0.4$ mV is very close to $\langle \Delta V_{TG}^{nnpn} \rangle$, but the average addition energy $\langle E_a^{pp'p} \rangle = 0.5 \pm 0.2$ meV is only half the value of $\langle E_a^{nnpn} \rangle$. The back gate capacitance in $pp'p$ is ~ 10 aF, indicating an island area of 50 nm by 700 nm, larger than (wl) (assuming the island extends over the entire ribbon width in the transverse direction). All average quantities were reproducible over multiple thermal cycles. Therefore the island formed in the $pp'p$ configuration is located in part under the TG, but extends to a larger area than the island in the npn case.

Coulomb blockade in the npn configuration was found in three other devices of different dimensions (A, C, E) where the npn regime could be accessed (the various devices exhibited different positions of the charge neutrality point). For device E , also the pnp configuration could be reached, where the measurement results are analogous to those for npn . The extracted $\langle \Delta V_{TG}^{nnpn} \rangle$ and $\langle E_a^{nnpn} \rangle$ for these devices are summa-

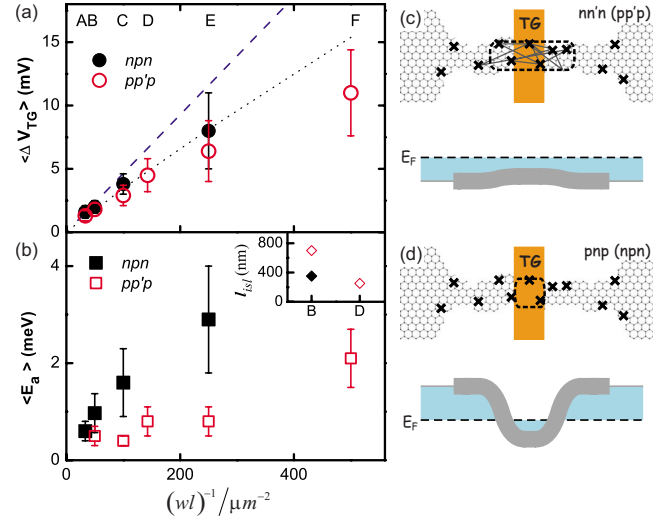


FIG. 4. (Color online) (a) Average peak spacing versus the inverse area of segment I, $(wl)^{-1}$, in the npn (black filled circles) and $pp'p$ (red open circles) configurations, for devices A through F as indicated. The blue dashed line is the peak spacing estimated by e/C_{TG}^{\parallel} , where C_{TG}^{\parallel} is a parallel-plate capacitance between the TG and GNR (see text). The values of e/C_{TG}^{\parallel} were also computed numerically by considering an island of area (wl) (black dotted line) (Ref. 20). (b) Average addition energy extracted from Coulomb diamonds measured in the npn (black filled squares) and $pp'p$ (red open squares) configurations versus $(wl)^{-1}$. The error bars in (a) and (b) represent standard deviation. Inset: the island size in the direction along the ribbon length (l_{isl}) for devices B and D in both npn (black filled diamonds) and $pp'p$ (red open diamonds) regimes extracted from the back gate capacitances. (c) and (d) Schematic illustrations of the device, with the \times symbol representing the scattering sites and the island enclosed in dashed lines. The underlying energy diagrams for the $nn'n$ (c) and pnp (d) regimes are also shown where the gray band represents the transport gap in the GNRs.

rized in Fig. 4(a) (black filled circles) and Fig. 4(b) (black filled squares), respectively. For all four devices, the measured $\langle \Delta V_{TG}^{nnpn} \rangle$ agrees quantitatively well with the numerically computed e/C_{TG}^{\parallel} (Ref. 20) by considering an island of size wl [black dotted line in Fig. 4(a)]. Moreover, both $\langle \Delta V_{TG}^{nnpn} \rangle$ and $\langle E_a^{nnpn} \rangle$ increase with decreasing area (wl) , consistent with the observation in device B , i.e., carriers are confined in segment I in the npn configuration.

Furthermore, we observed Coulomb blockade in the $pp'p$ regime in all six devices A to F . For devices A, B, E , we could also access the $nn'n$ configuration and the results are similar to those in the $pp'p$ case. For all devices, the average addition energy, $\langle E_a^{pp'p} \rangle$ in the $pp'p$ regime is much smaller than that in the npn case and does not vary much despite the differences in device dimensions (except for device F), as shown by the red open squares in Fig. 4(b) (no clear Coulomb diamonds were observed in device A in the $pp'p$ regime). In devices B and D , the measured back gate capacitance indicates that the island sizes are 50×700 nm² and 50×250 nm², respectively [Fig. 4(b) inset], significantly larger than the area of segment I. The capacitance of this large island to the relative narrow TG, $C_{TG}^{pp'p}$, is still roughly

the same as that for an island limited to segment I, so the peak spacings in $pp'p$ [Fig. 4(a), red open circles] are similar to those for npn .

The reproducible scaling of addition energy and peak spacing as a function of device dimensions is consistent with the results obtained from device *B*: when pn -junctions are induced by the TG and BG, an island is formed in between the junctions; without the pn -junctions, a much larger island is formed, presumably due to disorder. However, the source and drain capacitances are comparable (npn) or even larger ($pp'p$) than C_{TG} ,²¹ and contribute more than half of the total capacitance. This means that extracting the island size from E_a may be unreliable. For device *B* (npn and $pp'p$) and *D* ($pp'p$), we have measured the back gate capacitance, which gives an independent estimate of the island size [Fig. 4(b) inset] and is in agreement with our interpretation of the island size in the two regimes.

If islands are induced by disorder in the $pp'p$ case, there are likely to be disorder-induced islands in the npn case as well in addition to the islands formed by the pn junctions. Indeed evidence of multiple islands was observed experimentally in several cases (not shown). The presence of the additional islands contributes to the large spread in peak spacings and addition energies mentioned earlier.

These disorder-induced islands in the $pp'p$ regimes are five to ten times longer than the ribbon width, which could

be explained by Anderson localization, due to strong scattering at the rough ribbon edges as proposed in Refs. 22–26. This reveals a different aspect of the electronic properties of the GNRs compared to other work, where the extent of the island is found to be comparable with the ribbon width.^{14,27,28} Further studies are needed in order to clarify the underlying mechanisms behind the various observations.

In conclusion, a single electron transistor is formed in graphene nanoribbon devices with single top gates. Two pn -junctions at the two edges of the top gate induced by the top gate and back gate voltages act as barriers to form an island. Hundreds of Coulomb peaks were observed in this regime. In the absence of the pn -junctions, regular Coulomb blockade is also observed where the island can be induced by ribbon edge disorder. Observations from measurements of five other devices give consistent results. We anticipate that multiple top gates on a graphene nanoribbon will offer additional control for future device applications, and provide further insight into the electronic properties of graphene nanoribbons.

We thank K. Ensslin, M. Fogler, D. Goldhaber-Gordon, P. Kim, Y. Nazarov, C. Stampfer, and G. Steele for useful discussions, and L.P. Kouwenhoven for the use of a ³He system. This work was supported by the Dutch Foundation for Fundamental Research on Matter (FOM).

- ¹L. P. Kouwenhoven, C. M. Marcus, P. L. McEuen, S. Tarucha, R. M. Westervelt, and N. S. Wingreen, in *Mesoscopic Electron Transport*, edited by L. L. Sohn, L. P. Kouwenhoven, and G. Schön (Kluwer, Alphen aan den Rijn, the Netherlands, 1997).
- ²B. Trauzettel, D. V. Bulaev, D. Loss, and G. Burkard, *Nat. Phys.* **3**, 192 (2007).
- ³M. I. Katsnelson, K. S. Novoselov, and A. K. Geim, *Nat. Phys.* **2**, 620 (2006).
- ⁴A. K. Geim and K. S. Novoselov, *Nature Mater.* **6**, 183 (2007).
- ⁵C. Stampfer, J. Güttinger, F. Molitor, D. Graf, T. Ihn, and K. Ensslin, *Appl. Phys. Lett.* **92**, 012102 (2008).
- ⁶L. A. Ponomarenko, F. Schedin, M. I. Katsnelson, R. Yang, E. W. Hill, K. S. Novoselov, and A. K. Geim, *Science* **320**, 356 (2008).
- ⁷J. Güttinger, C. Stampfer, S. Hellmueller, F. Molitor, T. Ihn, and K. Ensslin, *Appl. Phys. Lett.* **93**, 212102 (2008).
- ⁸K. Nakada, M. Fujita, G. Dresselhaus, and M. S. Dresselhaus, *Phys. Rev. B* **54**, 17954 (1996).
- ⁹L. Brey and H. A. Fertig, *Phys. Rev. B* **73**, 235411 (2006).
- ¹⁰Y.-W. Son, M. L. Cohen, and S. G. Louie, *Phys. Rev. Lett.* **97**, 216803 (2006).
- ¹¹M. Y. Han, B. Özyilmaz, Y. Zhang, and P. Kim, *Phys. Rev. Lett.* **98**, 206805 (2007).
- ¹²X. Li, X. Wang, L. Zhang, S. Lee, and H. Dai, *Science* **319**, 1229 (2008).
- ¹³Z. Chen, Y.-M. Lin, M. J. Rooks, and P. Avouris, *Physica E* **40**, 228 (2007).
- ¹⁴C. Stampfer, J. Güttinger, S. Hellmüller, F. Molitor, K. Ensslin, and T. Ihn, *Phys. Rev. Lett.* **102**, 056403 (2009).
- ¹⁵K. S. Novoselov, A. K. Geim, S. V. Morozov, D. Jiang, Y. Zhang, S. V. Dubonos, I. V. Grigorieva, and A. A. Firsov, *Science* **306**, 666 (2004).
- ¹⁶J. B. Oostinga, H. B. Heersche, X. Liu, A. F. Morpurgo, and L. M. K. Vandersypen, *Nature Mater.* **7**, 151 (2008).
- ¹⁷P. G. Silvestrov and K. B. Efetov, *Phys. Rev. Lett.* **98**, 016802 (2007).
- ¹⁸G. A. Steele, G. Götz, and L. P. Kouwenhoven, *Nat. Nanotechnol.* **4**, 363 (2009).
- ¹⁹When the carrier density in segment I or II is low, we typically observe that low bias conductance vanishes and Coulomb diamonds overlap.
- ²⁰G. A. Steele, Ph.D. thesis, MIT, 2006.
- ²¹See EPAPS Document No. E-PRBMDO-80-R25936 for capacitance analysis and additional data on other devices. For more information on EPAPS, see <http://www.aip.org/pubservs/epaps.html>.
- ²²D. Gunlycke, D. A. Areshkin, and C. T. White, *Appl. Phys. Lett.* **90**, 142104 (2007).
- ²³Y. Yoon and J. Guo, *Appl. Phys. Lett.* **91**, 073103 (2007).
- ²⁴E. R. Mucciolo, A. H. Castro Neto, and C. H. Lewenkopf, *Phys. Rev. B* **79**, 075407 (2009).
- ²⁵M. Evaldsson, I. V. Zozoulenko, H. Xu, and T. Heinzl, *Phys. Rev. B* **78**, 161407(R) (2008).
- ²⁶D. Basu, M. J. Gilbert, L. F. Register, S. K. Banerjee, and A. H. MacDonald, *Appl. Phys. Lett.* **92**, 042114 (2008).
- ²⁷F. Sols, F. Guinea, and A. H. Castro Neto, *Phys. Rev. Lett.* **99**, 166803 (2007).
- ²⁸K. Todd, H.-T. Chou, S. Amasha, and D. Goldhaber-Gordon, *Nano Lett.* **9**, 416 (2009).